

Highlights

A Machine Learning Approach to Automate Ductile Damage Parameter Selection in Finite Element Simulations

A.N. O'Connor, P.G. Mongan, N.P. O'Dowd

- Material parameters obtained using Bayesian optimisation provide excellent agreement between simulated and experimental data.
- Ductile damage parameters are successfully derived for ambient and higher test temperatures.
- Required user-defined input such as test data can be easily obtained from standard engineering tests.

A Machine Learning Approach to Automate Ductile Damage Parameter Selection in Finite Element Simulations

A.N. O'Connor^{a,b}, P.G. Mongan^{a,c}, N.P. O'Dowd^{a,b,c}

^a*School of Engineering, University of Limerick, Ireland*

^b*Bernal Institute, University of Limerick, Ireland*

^c*Confirm Smart Manufacturing Research Centre, Ireland*

Abstract

A key limitation of finite element analysis of material behaviour is accurate modelling of material damage. Here Bayesian optimisation, a machine learning technique, is shown to successfully identify material model parameters in a commonly used ductile damage model. The Bayesian derived material model parameters result in simulated output with less than 2% error compared to experimental data. The framework detailed here is fully autonomous, requiring data that can be derived from a simple tensile test. This framework has been successfully deployed to three datasets of P91 material tested at ambient (20 °C) and higher (500 °C) temperatures.

Keywords: machine learning; Bayesian optimisation; ductile damage; parameter selection;

Email address: alison.oconnor@ul.ie (A.N. O'Connor)

1. Introduction

The tensile test is a standard test method [1] that provides information about the mechanical properties of metallic materials. In cases where experimental data are limited finite element (FE) simulations can be used to simulate the mechanical behaviour of materials and examine hypotheses that cannot be experimentally investigated. The FE method offers a level of detail not obtainable from analytical solutions but is relatively computationally expensive and ultimately relies on experimental data for validation. Ductile damage modelling can be used in conjunction with FE simulations to represent mechanical behaviour of metals under high strain conditions when damage mechanisms are important [2–4]. Such models are generally complex and require calibration parameters that are difficult to derive experimentally or analytically. Calibrating a ductile damage modelling can be considered a form of black box optimisation, where the inputs (calibration parameters) and outputs (data in a tensile test) are known but the functional relationship between the calibration parameters and the material mechanical response is unknown. Such an optimisation problem can be solved using machine learning, a term used to describe algorithms and/or statistical models that allow computers to select the best method of progression in a problem, without human interaction or explicit programming [5]. In particular, Bayesian optimisation (BO) has been shown to outperform other machine learning algorithms in solving black box optimisation problems [6]. Machine learning algorithms, informed directly by experimental and/or simulation data, have been successfully employed to solve numerous engineering problems across a wide range of applications [7–9]. BO is commonly used in machine learning

for artificial neural network (ANN) hyperparameter selection [5, 7, 10, 11] and has recently been used to identify material parameters in a viscoplastic material model, Ryan et al. [12]. The versatility of BO makes it an attractive method for solving a wide variety of engineering challenges such as: material design [13, 14], cardiac mechanics [15], light emission for thin films [16] and manufacturing process improvements [7, 17]. In [2, 3, 18, 19] ANNs have been used to assess damage model parameters. However, ANNs require a significant number of FE simulations to ‘train’ the model to recognise correlations and relationships between input values and results which is computationally expensive. This work demonstrates how BO can be used to automatically identify the material damage model parameters that best match experimental data from a tensile test, reducing the time associated with deriving parameter values and requiring minimal user intervention. A similar approach to that used in Ryan et al. [12] has been adopted, but in this case the approach is applied to ductile damage, using a Gurson model, rather than the rate sensitive viscoplasticity constitutive models examined in Ryan et al. [12].

2. Material behaviour in FE simulations

A tensile test consists of a standardised specimen geometry that is loaded in one direction until complete separation of the specimen. Data are typically expressed in terms of engineering stress and strain (σ_{eng} and ϵ_{eng} , respectively), where stress and strain are derived from test measurements of test machine load and specimen displacement, respectively. For metals the relationship between stress and strain typically comprises three regions (see

Figure 1): a linear region, a strain hardening region where stress increases non-linearly with strain, and a material damage region where stress decreases non-linearly with increasing strain. Several key mechanical properties derived from a tensile test are illustrated in Figure 1. The yield strength (σ_y) defines the stress at which material behaviour becomes non-linear. The linear region comprises data preceding the yield point of the material and the material stiffness or Young's modulus (E) is the slope of the stress-strain curve, as shown in Figure 1. Beyond σ_y the slope of the stress-strain decreases and a local geometrical discontinuity known as a 'neck' forms in the tensile specimen. The ultimate tensile strength, σ_{UTS} , denotes the maximum stress reached in the tensile test; beyond which the specimen's load bearing capacity degrades. The strain hardening region occurs for $\sigma_y \leq \sigma \leq \sigma_{UTS}$, as illustrated in Figure 1, and depicts a non-linear stress-strain relationship. The con-

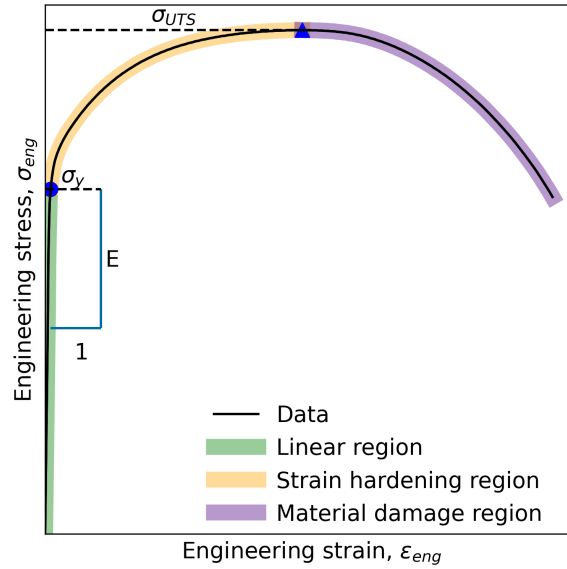


Figure 1: Illustration depicting material behaviour during tensile test experiment.

version from a load-displacement curve to an engineering stress-strain curve (Equations 1 and 2) used in Figure 1, assumes that the specimen geometry does not change during the test.

$$\sigma_{eng} = \frac{P}{A} \quad (1)$$

$$\varepsilon_{eng} = \frac{\Delta l}{l_o} \quad (2)$$

Where P represents the force applied to the specimen, A the specimen cross-sectional area, Δl the change in length of the specimen and l_o the original length. However, as the specimen is stretched in the loading direction, it reduces in thickness in the direction transverse to the load, due to the Poisson effect [20]. Therefore, the cross-section area of the specimen decreases continuously with increasing load. To account for this geometric change a so-called true stress-true strain relationship (denoted as σ_{true} and ϵ_{true} , respectively) is formulated from engineering stress-strain data, as shown in Equations 1 to 4 [20].

$$\sigma_{true} = \sigma_{eng} (1 + \varepsilon_{eng}) \quad (3)$$

$$\varepsilon_{true} = \ln(1 + \varepsilon_{eng}) \quad (4)$$

This equation becomes increasingly inaccurate as the neck develops due to the non-uniformity of stress and strain in the neck. Therefore, in this work for $\sigma > \sigma_{UTS}$, the true stress is interpolated from the values for $\sigma \leq \sigma_{UTS}$, with the understanding that, in the absence of damage, the true stress always increases with increasing strain. Here, a linear relationship between true

stress and true strain, with slope m , for $\sigma \geq \sigma_{UTS}$ is assumed. The parameter m is unknown and is calibrated as part of the BO, as discussed later.

2.1. The damage model

A popular damage model, used to describe the softening behaviour seen in the material damage region of Figure 1, is the Gurson-Tvergaard-Needleman (GTN) model [3, 21, 22]. The parameters are typically estimated by conducting numerical simulations, manually iterating the relevant parameter value, and matching the simulation result to experimental data.

The GTN model response for a tensile test is described in Equation 5, where σ is the current (uniaxial) stress, σ_y is the material yield strength, f is the current void volume fraction (the ratio of the volume of voids to the total material volume) and q_1 , q_2 , and q_3 are material parameters,

$$\left(\frac{\sigma}{\sigma_y}\right)^2 + 2q_1f \left(\cosh \frac{q_2\sigma}{2\sigma_y}\right) - q_3f^2 = 1. \quad (5)$$

The rate of change of the void volume fraction, \dot{f} , is described by Equation 6 where \dot{f}_n and \dot{f}_g represent the void nucleation rate and void growth rate, respectively,

$$\dot{f} = \dot{f}_n + \dot{f}_g. \quad (6)$$

The void growth rate, \dot{f}_g , is obtained from conservation of mass,

$$\dot{f}_g = (1 - f)\dot{\varepsilon}, \quad (7)$$

while the void nucleation rate, \dot{f}_n , is given by Equation 8, where ε_m^p is the plastic strain of the unvoided (matrix) material, and f_N , S_N and ε_N , are material parameters.

$$\dot{f}_n = \frac{f_N}{S_N \sqrt{2\pi}} \exp \left[-\frac{1}{2} \left(\frac{\varepsilon_m^p - \varepsilon_N}{S_N} \right)^2 \right] \dot{\varepsilon}_m^p, \quad (8)$$

Since, the void volume, f , is defined through a rate equation, the initial void volume fraction, f_0 , must also be defined. Hence, there are a total of seven parameters in the GTN ductile damage model to fit using BO: q_1 , q_2 , q_3 , S_N , f_N , ε_N , and f_0 . Including the slope of the true stress-true strain curve for $\sigma > \sigma_{UTS}$, m , gives a total of eight parameters.

3. The Bayesian Optimisation Framework

The goal of BO is to find the global minimum of an unknown (black box) function. There are two key ingredients to a BO framework: a surrogate model and a loss function. The surrogate model, sometimes called a probabilistic model, describes the BO's current knowledge about the unknown function based on observed data. The loss function describes how well the previously observed data are optimised (i.e. converging towards a global minimum) [23]. The surrogate model and loss function work jointly with an acquisition function, which controls how the BO explores the parameter space. The surrogate model, $f(x)$, is determined using Gaussian process regression (GPR) on inputs, x , the observed data related to the unknown function. A Gaussian process is a collection of random variables, many of which have consistent, joint Gaussian distributions, specified by the covariance function [24, 25] (see Section 3.1 for further details on the covariance function).

The probability distribution generated by GPR is based on a ranking system, where input x is evaluated as $f(x)$ and $f(x)$ is ranked in terms of

its performance relative to the loss function. In this work the loss function is the mean average percentage error (MAPE) which quantifies the similarity between simulated and experimental data (see Section 3.2 for further detail). To minimise the loss function the L-BFGS-B optimisation algorithm [27] is used. This algorithm uses historical gradient evaluations of $f(x)$ to construct an approximation of the unknown function.

In order to set reasonable bounds to the possible solutions of the problem, a parameter space is defined, within which the BO algorithm searches for values. The parameter space of the current problem is defined in Table 1 for the GTN parameters, based on information in the literature for similar materials [28–30]. The process used to define the bounds for m is outlined in detail in Section 4.

3.1. The covariance function

The covariance function used in the GPR has significant influence on the shape and characteristics of the surrogate function [7]. In this work a covariance function, $k(x_i, x_j)$, which uses a combination of the Matérn, Constant and White noise (White) functions, as shown in Equation 9, is implemented,

$$k(x_i, x_j) = \text{Matérn} + \text{Constant} \times \text{White}. \quad (9)$$

As the shape and/or characteristics of the black box function are unknown this covariance kernel is designed to account for shifts in mean position (Constant), noise (White) and to model potentially multiple minima positions (Matérn). Specifically, the Matérn covariance function is defined in Equa-

Table 1: Parameter space representing the minimum and maximum boundary for each parameter

Dataset	Parameter	Minimum	Maximum
1-3	q_1	9.00×10^{-1}	1.60
1-3	q_2	9.00×10^{-1}	1.10
1-3	q_3	8.10×10^{-1}	2.56
1-3	ϵ_N	2.50×10^{-1}	4.00×10^{-1}
1-3	f_N	3.00×10^{-1}	9.00×10^{-2}
1-3	s_N	1.00×10^{-1}	2.00×10^{-1}
1-3	f_0	1.30×10^{-3}	1.50×10^{-3}
1	m	0	800
2	m	0	1100
3	m	0	800

tion 10 [31],

$$k(x_i, x_j) = \frac{1}{\Gamma(\nu) 2^{\nu-1}} \left(\frac{\sqrt{2\nu}}{l} d(x_i, x_j) \right)^\nu K_\nu \left(\frac{\sqrt{2\nu}}{l} d(x_i, x_j) \right). \quad (10)$$

In Equation 10 x_i and x_j are input points, d is the Euclidean distance, K_ν is a modified Bessel function and Γ is the gamma function.

The Constant covariance function, is defined in Equation 11 [31],

$$k(x_i, x_j) = C; \forall x_i, x_j, \quad (11)$$

where C is a constant.

The White covariance function is defined in Equation 12,

$$k(x_i, x_j) = \sigma^2 \delta_{ij}, \quad (12)$$

where σ^2 is constant and δ_{ij} the Kronecker delta function. In this work the following hyperparameters are fixed: $\nu = 1$, $l = 1$, $C = 1$, $\sigma^2 = 1$ with the bounds, for each kernel hyperparameter, restricted to: $(1 \times 10^{-5}, 1 \times 10^5)$. the white function seems very simple and not very different from a constant. I'm not sure how that is supposed to represent noise The white noise function adds noise on the diagonal of the matrix to account for uncertainty in data. If input values for kernel are identical ($x_i == x_j$) then the matrix will have a valid of 1 on the diagonal, else it be 0. For FE simulations this may relate to uncertainties in stresses due to meshing or model assumptions. The constant kernel does not depend on inputs. It's main use is to check for bias in the model. By adding a constant to the kernel matrix the model should become less sensitive to small changes in the input values - the idea behind this is that it will improve the numerical stability of the GPR.

I don't understand - your define hyperparameters and then you define bounds

3.2. The loss function

The aim of this work is to minimise the difference between experimental test data and simulation outputs generated from a finite element (FE) analysis of the problem. The experimental data are measures of applied load and specimen extension taken in-situ. In this work mean average percentage error (MAPE), Equation 13, is used to measure the similarity between experimental data and simulated output.

$$\text{MAPE} = \frac{100}{n} \sum_i^n \left| \frac{P_{exp}^i - P_{sim}^i}{P_{exp}^i} \right|. \quad (13)$$

Here P_{exp}^i represents each experimental load data point, P_{sim}^i is the corresponding simulation load and n the number of data points. MAPE provides an average measure of error over the full dataset with all data points equally weighted.

3.3. The acquisition function

In this work the upper confidence bound (UCB) acquisition function is employed. The UCB, Equation 14, identifies the new parameters through a weighted sum of the surrogate function, where $\mu(x)$ is the mean, and $\sigma(x)$, the variance, respectively [23, 32]. You've previously used σ as variance variance and uncertainty used interchangeably. Have confirmed it is variance modified accordingly.

$$\alpha_{UCB}(x) = \mu(x) + \sigma(x). \quad (14)$$

Exploration and exploitation balance how the model searches the parameter space. When B is large the acquisition function operates in exploratory mode; reducing the weight switches the model to exploitation mode. Is the weight B or square root of B ? The weight is square root of B but others often replace this with Beta symbol as shown above In exploration mode the new assessment point differs significantly from the previous iteration; exploratory mode returns a new assessment point close to that tested previously. In our work we have taken $B = 2.5$.

In addition to the weight, B , the acquisition function has two further hyperparameters: the number of random samples, N_R , and the number of optimisation samples, N_O . N_R controls the size of the array over which the range

of possible inputs are distributed—increasing N_R increases the precision of the GPR, thus reducing uncertainty. N_O defines how many evaluations of the acquisition function are conducted and controls the level of uncertainty in the acquisition function—increasing N_O makes the optimisation process more robust. Not sure what ‘—’ means

3.4. Initialising the BO framework

BO requires a database of initial evaluated data within the parameter space. We use a design of experiment (DoE) approach, [33, 34], to provide the initial evaluated data. DoE maximises the statistical significance of results with a minimised number of experiments. Table 2 shows a DoE array for 12 initial finite element simulations based on the maximum and minimum parameter space values, where values of 1 and 2 in Table 2 represent the minimum and maximum parameter bounds, respectively.

Figure 2 shows a flowchart describing the DoE procedure. As illustrated in Figure 2, the user first defines the parameter space (here shown in Table 1). A DoE array (Table 2) is defined and the array is then modified so that the minimum and maximum values are replaced by the user-defined parameter values. A finite element simulation is conducted for each row of the DoE array (i_{max} is the number of (virtual) experiments in the DoE array, here 12). Results from the simulation are processed and the experiment data are compared to the simulation data, and the MAPE is calculated. After each analysis, i , the parameter values and the associated error measurement are appended to a csv file. note: these are not mathematical iterations but are computing iterations! - check the definition on wikipedia, Iteration: the repetition of a process to generate a sequence of outcomes. I’m not clear

Table 2: Design of experiments array for 8 parameters with each parameter at 2 levels.

	P_1	P_2	P_3	P_4	P_5	P_6	P_7	P_8
1	1	1	1	1	1	1	1	1
2	1	1	1	1	1	2	2	2
3	1	1	2	2	2	1	1	1
4	1	2	1	2	2	1	2	2
5	1	2	2	1	2	2	1	2
6	1	2	2	2	1	2	2	1
7	2	1	2	2	1	1	2	2
8	2	1	2	1	2	2	2	1
9	2	1	1	2	2	2	1	2
10	2	2	2	1	1	1	1	2
11	2	2	1	2	1	2	1	1
12	2	2	1	1	2	1	2	1

on where I'm misusing the word iterate? remove the box around the text
 "Proceed..." in the figure. done

3.5. Implementation of the BO-Finite element model

The output of the DoE in Figure 2 (a csv file of parameter values and error measurements) is used to initialise the Bayesian optimiser. Figure 3 outlines the method: The DoE data are analysed by the GPR to create an initial surrogate model. GPR outputs are then provided to the acquisition function which identifies new parameter values based on ranking the DoE data. A new finite element simulation, using parameter values obtained

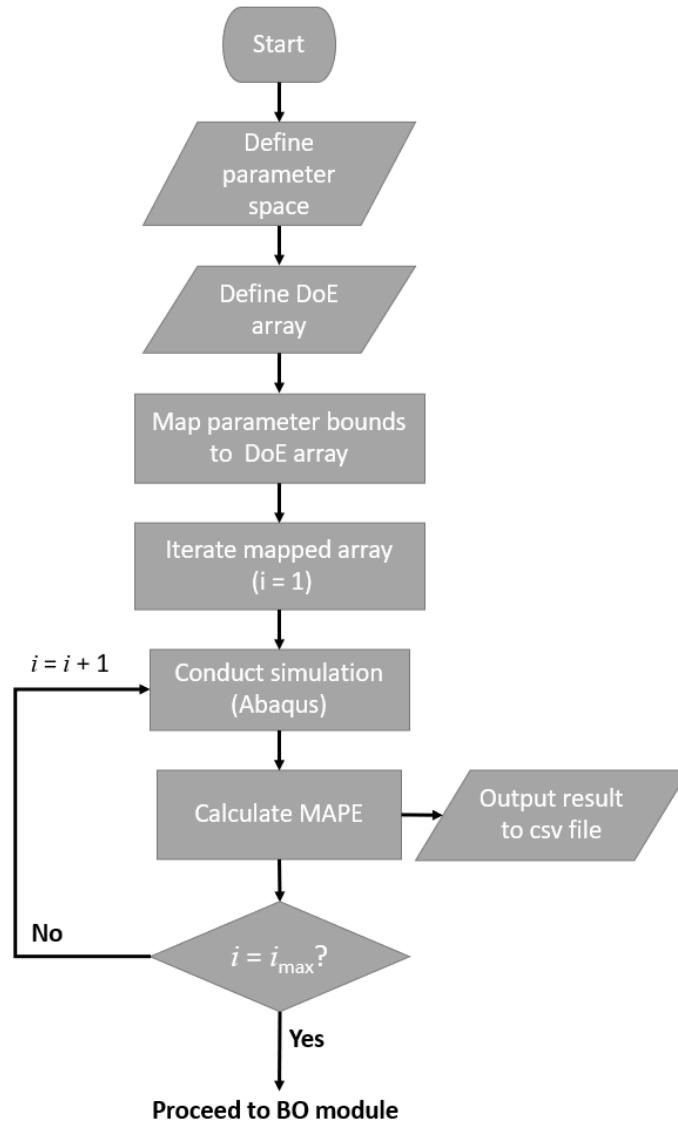


Figure 2: Flowchart demonstrating the design of experiments code procedure (prior to bayesian optimisation).

from the acquisition function, is then conducted. Again simulation data is compared to the experiment and the MAPE is calculated. Acquisition function parameter values and error measurement data are appended to the existing csv file. *please reorganise spacing to avoid double spacing after periods. I will continue to do this* The algorithm iterates until the MAPE is less than 2% or a maximum number of iterations (j_{max}) is achieved. In the current approach, to ensure that BO is always carried out the analysis is not terminated if MAPE is less than 2% in the DoE.

4. Experimental Tensile Tests

The three experimental tensile test results are shown in Figure 4 for the material of interest (P91, a piping steel). Datasets 1 & 2 were conducted under identical test conditions. Therefore Dataset 2 can be considered a ‘repeat’ test result. Load-displacement data were converted to true stress-strain by limiting data to the range below the maximum load.

The ultimate tensile strength (σ_{UTS}) was defined as the true stress corresponding to the maximum load. The second derivative of true strain was calculated using a Savitzky-Golay filter with a three degree polynomial fit.

4.1. Assessment of linear data

To ensure the yield strength was accurately defined the size of the filter window (i.e. the number of data points over which the polynomial is applied) was solved iteratively. For each iteration (i.e. each window size) the yield strength (σ_y) was defined as the position of the inflection point. The ‘best’ yield strength was selected as a function of the error (between the predicted linear region and the experimental linear region), the overall fit of the linear

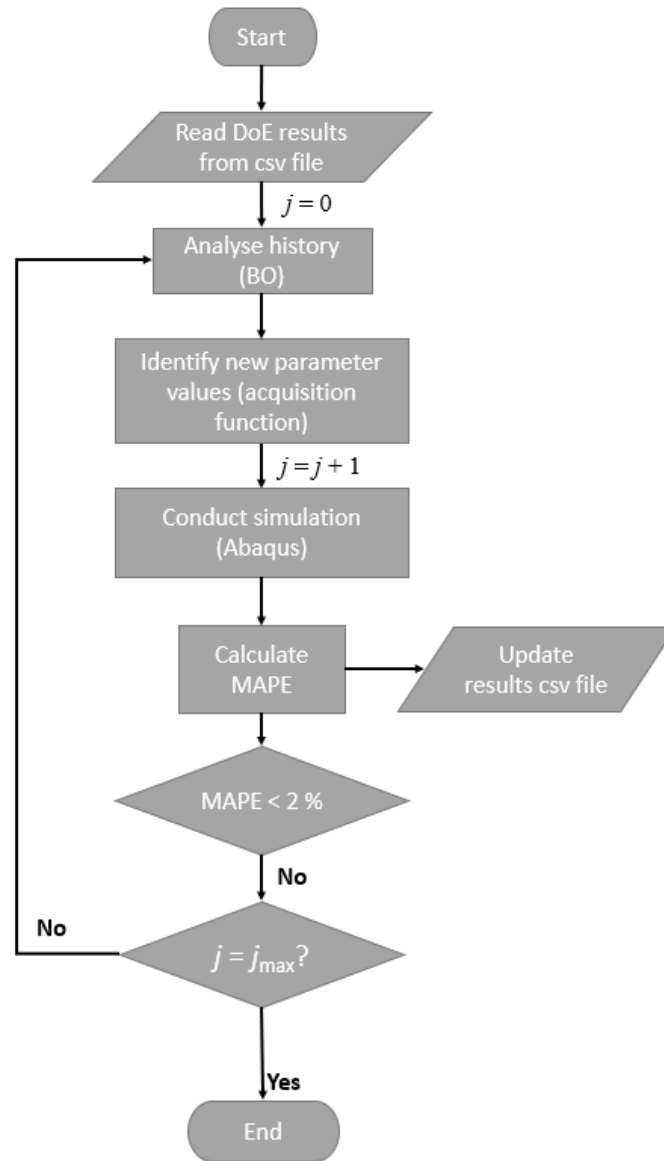


Figure 3: Flowchart depicting code procedure for Bayesian optimisation.

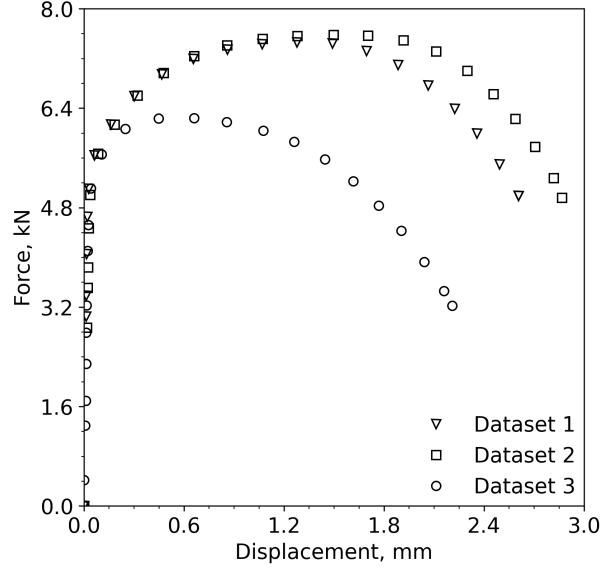


Figure 4: Experimental tensile test results for P91 material at test temperatures of 20 °C (Datasets 1 and 2) and 500 °C (Dataset 3). Note: Markers are placed as specific intervals for data visibility purposes. Higher data acquisition rate was used during testing.

region (r^2) and the estimated yield strength value. Young's modulus was calculated by employing linear regression to fit all data below the proposed 'best' yield strength. Figure 5 shows the result of the assessment for each of the three datasets.

To extrapolate data beyond σ_{UTS} a linear relationship between stress and strain was assumed. The slope of the extrapolated line, parameter m , is a searchable parameter that the BO framework will derive. The maximum value of parameter m was ascertained from experimental data by applying a linear fit to groups of data preceeding the σ_{UTS} position. The first fit was applied to a single pair of data points immediately adjacent to the σ_{UTS} position, the second fit was applied to the previous pair plus an additional

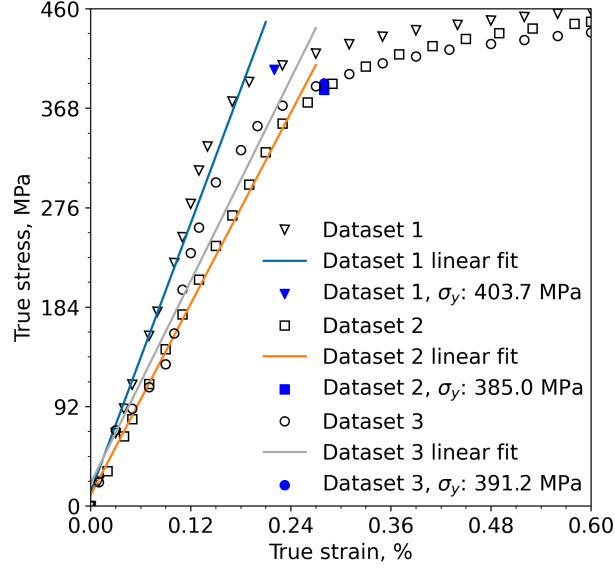


Figure 5: True stress - true strain relationship for three experimental tests.

data point, the third fit was applied by expending the second group by an additional data point and so on. This method was applied up to a maximum of five data points preceding the σ_{UTS} position. Parameter m was assessed for each linear fit and the largest value was selected to represent the maximum parameter boundary. True stress-true strain data were extrapolated based on the assumption that the extrapolated line must pass through the σ_{UTS} position with a slope of parameter m . Figure 6 shows the extrapolated data for the parameter space of dataset 1.

5. FE Modelling of Tensile Tests

Finite element modelling was conducted using Abaqus 2021 [30]. Analyses were conducted using Abaqus/Explicit, a dynamics based solution, with a mass scaling factor of 10 to reduce computation time. The model was meshed

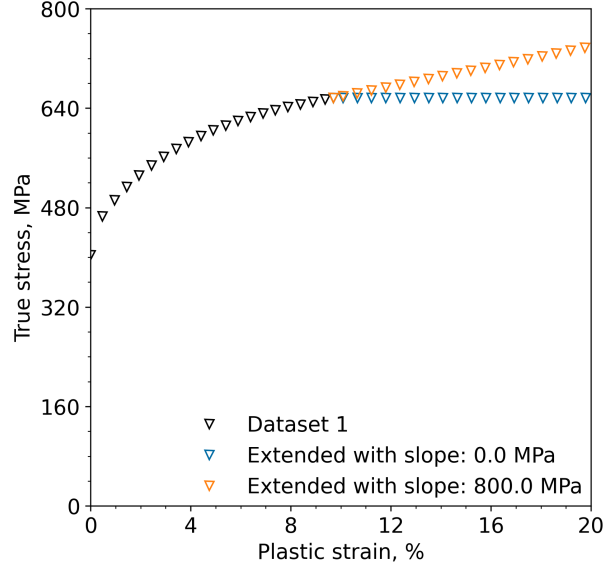


Figure 6: True stress - plastic strain relationship for dataset 1. Test data are shown using black markers. Two parameter values (minimum and maximum) are distinguished using coloured markers.

using axisymmetric elements. A total of 4664 elements were used. Each element in the gauge section represents approximately 0.09 mm.

The experimental tensile test geometry was represented as shown in Figure 7. The use of a 2D geometry reduces the computational expensive associated with the simulation. To predispose the FE model to neck in the central gauge length a small imperfection was introduced to the bottom right hand corner as shown in Figure 7.

Boundary conditions were applied along the symmetry planes (shown by the red dashed lines in Figure 7). A reference node (red point shown in Figure 7) was coupled to the surface of the geometry and loading was applied through displacement control.

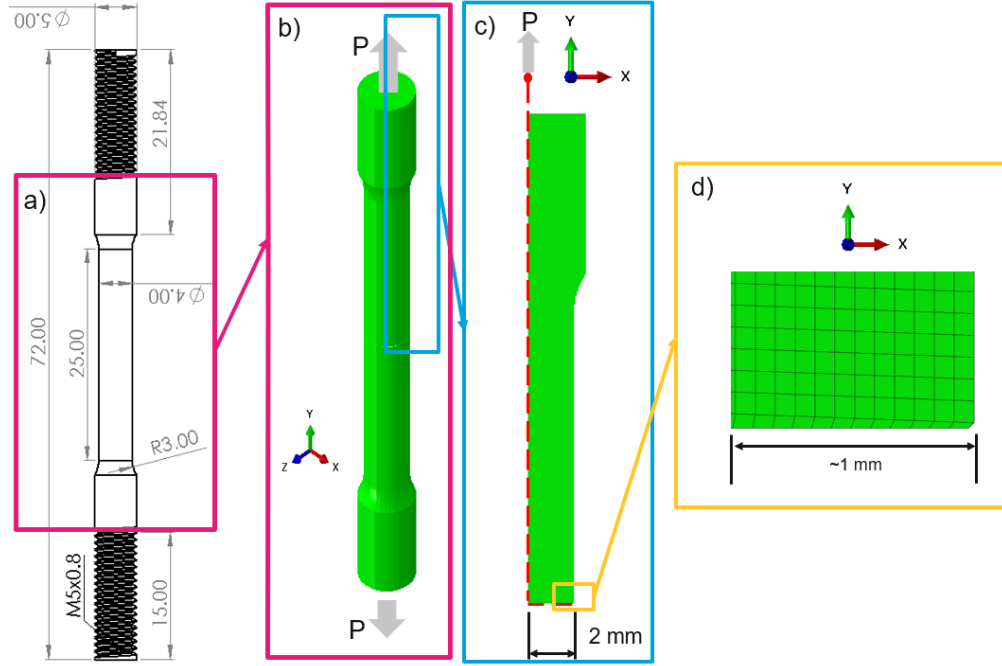


Figure 7: Illustration demonstrating the axisymmetric FE model. A small imperfection, shown in the yellow highlighted region, was modelled to ensure failure occurred in the midsection of the gauge length.

Within the FE simulation linear material behaviour was defined using the E and Poisson's Ratio ($\nu = 0.3$). Non-linear material behaviour was provided as an array of plastic strain versus true-stress (*PLASTIC in Abaqus). To model material degradation due to ductile damage the GTN model was applied (see Section 2.1).

Displacement data was taken from the reference node shown in Figure 7. The applied load was calculated by summing the vertical reaction force in elements located along the X symmetry plane.

6. Results and Discussion

As discussed, three data sets have been analysed. The minimum MAPE selected is 2% and the procedure described in Figure 3 is applied until this MAPE is reached. Abaqus simulations are preformed in sequence with 4 CPUs. Typically, this framework requires at least 150 finite element simulations with the full parameter selection taking approximately 4 hours. The framework was executed on a laptop with 4 Intel i7 CPUs and 32 gigabytes of RAM. Not all CPUs are required for the framework, other applications (e.g. Microsoft office) are sufficiently supported while the framework runs in the background. The lowest MAPE, 1.56 %, was found for dataset 1.

The comparison between data and simulation is shown in Figure 8 for the three datasets. Figure 8a shows that the simulated output is in good agreement with experimental data over the full displacement range although simulated forces are slightly underestimated compared with the experiment in the range $1.3 \leq \Delta u \leq 2.2$ mm. Similarly Dataset 2 (Figure 8b) shows good agreement between simulated and experimental data. For $\Delta u \geq 2.5$ mm simulated results for Dataset 2 slightly overestimate the force compared to the experiment. The overestimation is most notable at the final displacement point.

The parameter values selected by the BO framework are provided in Table 3 for each of the three datasets analysed.

The datasets analysed are for the same batch of material. The tests for dataset 1 and 2 have been carried out under identical conditions, while the test for dataset 3 has been carried out at a different temperature. The statistical nature of materials testing, often termed material scatter, has been

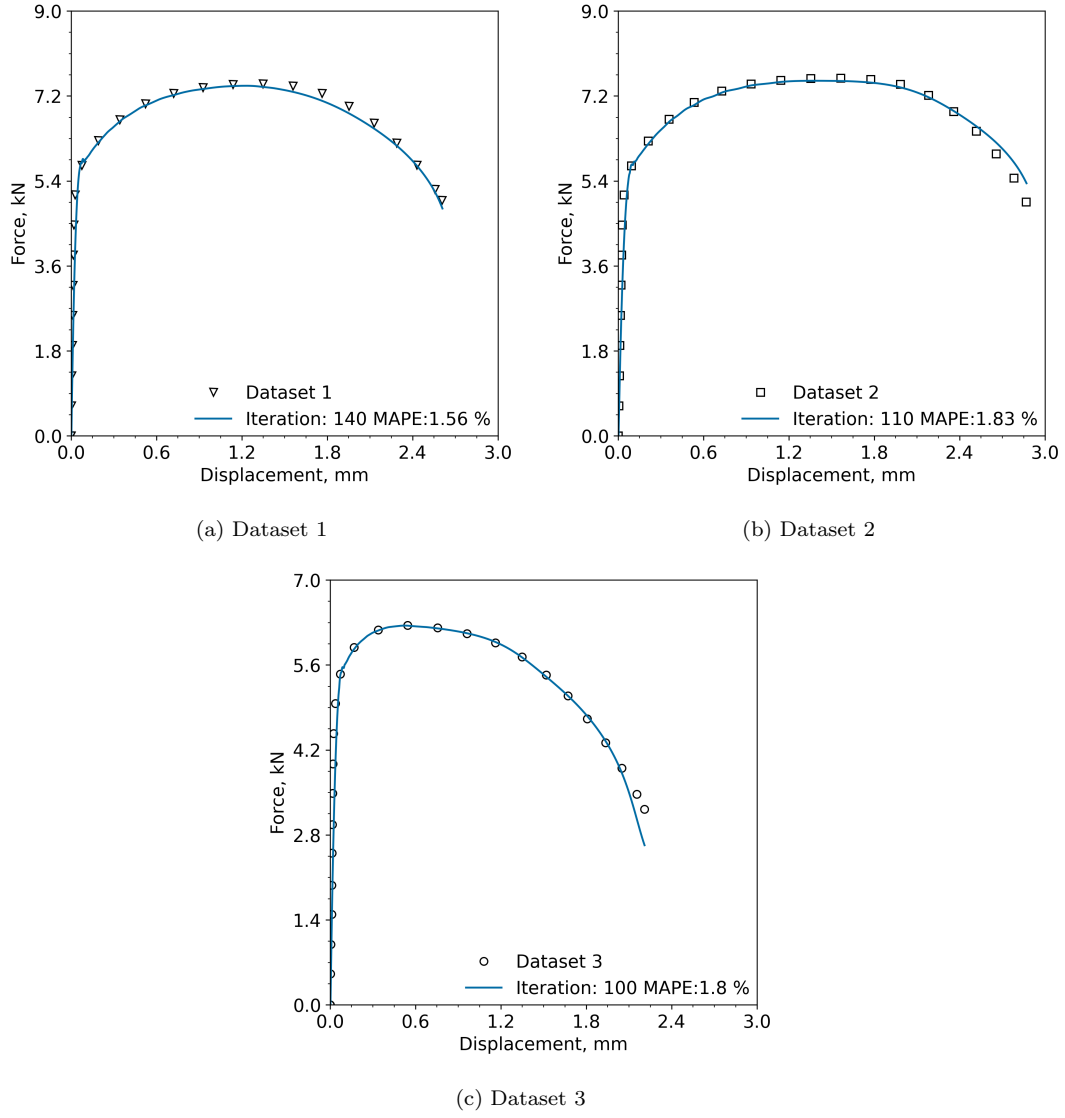


Figure 8: Comparison of experimental test data to simulated output for Dataset 1 (8a), Dataset 2 (8b), and Dataset 3 (8c). Parameter values are shown in Table 3.

Table 3: Bayesian optimisation framework parameter values for each of the three datasets analysed.

Parameter	Dataset 1	Dataset 2	Dataset 3
N_O		500	
N_R		50,000	
q_1	1.332	1.168	1.182
q_2	9.952×10^{-1}	9.667×10^{-1}	9.699×10^{-1}
q_3	2.295	1.407	2.001
ϵ_N	2.900×10^{-1}	3.467×10^{-1}	3.720×10^{-1}
s_N	1.671×10^{-1}	1.856×10^{-1}	1.214×10^{-1}
f_N	3.869×10^{-2}	8.481×10^{-2}	4.706×10^{-2}
f_0	1.370×10^{-3}	1.340×10^{-3}	1.310×10^{-3}
m	534.1	725.4	421.4
MAPE	1.563	1.827	1.799
N_j	140	110	100

widely acknowledged in the field of material science [35]. Given the difficulty in experimentally deriving material values and considering the statistical nature of material performance, it may be that machine learning methods such as the ones employed here are more appropriate for defining such parameters. It is interesting to note that parameter m , the slope of the extrapolated true stress-true strain curve was found to differ significantly between datasets 1 and 2. The optimised parameter m for datasets 1 was found to be 534 MPa while that for dataset 2 was found to be 725 MPa. Both datasets were tested

under identical conditions and, as shown in Figure 4, are broadly similar up to a displacement of ≈ 1.3 mm after which they begin to diverge.

It is also interesting to note that for all three datasets the parameter f_0 , representing the initial void volume fraction of the material are very similar. Generally the initial void volume fraction is assumed to be applicable to all test samples taken from a single batch of material which is consistent with what is observed here. However, comparing parameters ε_N , S_N and f_N across the three datasets presented in Table 3, there are significant differences. These parameters control how many voids nucleate under a given loading condition and, as such, are expected to be material specific rather than specimen specific.

In terms of the fitting parameters (q_1 , q_2 and q_3) it is common practise among the engineering community to fix $q_3 = q_1^2$ [36–38] this is based on assumptions made in the original model [39]. In this work q_3 was not constrained as a function of q_1 . Interestingly, despite the freedom of the BO framework to select any value of q_3 , Table 3 shows that dataset 2 found a value of $q_3 = 1.4071$ which is analogous to $q_1^2 = 1.3652$. Other fitting parameters (q_1 and q_2) are broadly similar when comparing across datasets. Given the complex nature of the material model and the close relationship between some parameters it is difficult to state with any certainty what impact any individual parameter has had on simulated output.

6.1. Effect of varying BO hyperparameters

To assess the effect of hyperparameter selection on the model parameters multiple analyses on dataset 1 were preformed. For each analysis the number of random and/or optimisation samples (N_R and N_0 , respectively)

were reduced as shown in Table 4. Reducing N_R reduces the precision of the input parameters which increases model uncertainty. The N_O defines how many evaluations of the acquisition function are conducted, this controls the level of uncertainty specifically related to the acquisition function. Results are plotted in Figure 9.

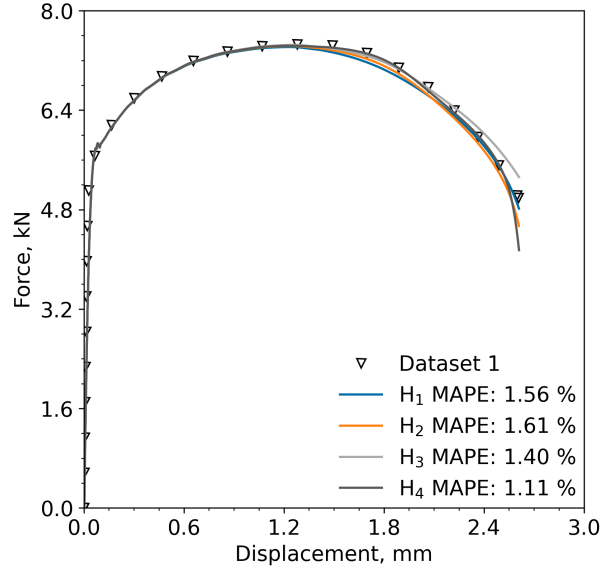


Figure 9: Plot of force versus displacement showing experimental data and simulated output for various hyperparameters.

Figure 9 shows that excellent agreement with experimental data is achieved for the four different hyperparameter choices but, it may be noted from Table 4 that the model parameters can depend significantly on hyperparameter selection. Given that excellent agreement was achieved for all four analyses this implies that the problem does not have a unique solution. That is to say that multiple combinations of the eight model parameters potentially provide good agreement to experimental data.

Table 4: Bayesian optimisation framework parameter values for dataset 1. The effect of hyperparameter settings on GTN parameter values.

Parameter	H_1	H_2	H_3	H_4
N_O	500	100	500	100
N_R	50,000	50,000	10,000	10,000
q_1	1.332	1.178	1.291	1.158
q_2	9.952×10^{-1}	1.021	9.547×10^{-1}	1.037
q_3	2.295	1.344	2.254	1.070
ϵ_N	2.900×10^{-2}	3.598×10^{-1}	3.519×10^{-1}	3.331×10^{-1}
s_N	1.671×10^{-1}	1.580×10^{-1}	1.001×10^{-1}	1.234×10^{-1}
f_N	3.869×10^{-2}	5.769×10^{-2}	3.086×10^{-2}	7.594×10^{-2}
f_0	1.370×10^{-3}	1.431×10^{-3}	1.412×10^{-3}	1.309×10^{-3}
m	534.1	542.8	514.5	621.9
MAPE	1.563	1.614	1.398	1.105
N_j	140	133	46	130

The lowest MAPE, 1.11% was found for analysis H_4 where N_R and N_O were 10,000 and 100, respectively. Comparing the model parameters (q_1 , q_2 etc.) for the four analyses shows that H_4 deviates considerably from H_1 . H_1 , as it has the highest N_R and N_O , is considered the most precise of the analyses investigated here. Comparing parameter m in analyses H_1 (534.13 MPa) and H_4 (621.85 MPa) shows a difference of almost 100 MPa. In terms of the expected change, and considering the parameter range, the deviation across analyses is significant. It is therefore not unexpected that

the remaining parameter values, those specific to the GTN model, also differ. This outcome supports the non-uniqueness of the problem.

Comparing H_1 and H_2 in Table 4 indicates how reducing N_O affects the analysis. While individual model parameters change slightly, overall both analyses provide similar measures of MAPE and result in load-displacement traces similar to the experimental data (Figure 9). It should be noted that H_2 resulted in a slightly higher MAPE, 1.61%, compared to that of H_1 , 1.56%. The higher measure of MAPE for H_2 is as expected given that the reduced N_O effectively reduces the amount of statistical information known about the black box function resulting in less accuracy.

Comparing H_1 and H_3 in Table 4 enables the effect of reducing N_R to be assessed. Here it is shown that fitting parameters q_1 , q_2 and q_3 are broadly similar. Other parameters, specifically nucleation related terms s_N and f_N , exhibit differences with H_3 having smaller values compared to H_1 . The effect of the reduction in these parameters is also notable in Figure 9 where comparing H_1 and H_3 shows that H_3 deviates from H_1 at $2.0 \leq \Delta \leq 2.7$ mm. In essence the lower nucleation parameters seen in analysis H_3 reduced the nucleation of new voids thus giving a lower rate of damage compared to H_1 . On the whole comparing H_1 and H_3 indicates that reducing N_R did not significantly affect the model output. In fact comparing H_1 and H_2 to H_3 shows that lower N_R provided a more accurate result (i.e. lower MAPE) in a significantly shorter timescale (iteration number 46). While this may appear initially surprising it simply means that lower values of N_R did not overtly effect the mean calculation of the block-box function. Analysis H_4 shows output associated with a reduction in both the N_O and N_R . Interestingly

H_4 has the lowest MAPE, 1.11%, however the number of iterations (130) is similar to those required for the H_1 and H_2 analyses.

It is difficult to state with any certainty which, if any, of the analyses in Table 4 would be considered the most ‘appropriate’. The issue of non-uniqueness in GTN model parameter values has been highlighted by others [3, 28]. One method of limiting the GTN parameters is to introduce other, cracked, specimen geometries such as single edge notch bend (SENB) or compact tension (CT) geometries. Cracked geometries are subject to considerable local stress triaxiality that inhibits plastic flow and promotes void growth [40]. As the GTN model, Equation 5, is not specimen specific the parameters of the model should be equally applicable to a uni-axial tensile geometry or a fracture toughness geometry (e.g. SENB or CT geometry). Theoretically one could integrate several types of geometry to the framework developed here to limit the number of parameter combinations. However, the introduction of a cracked geometry causes several complications. Numerical simulations of cracked geometries often require contact interactions and specialist meshing techniques which increases model complexity and computational demand. While this is certainly within the ability of modern computing ability the increase in computational demand would inevitably increase the required time for BO to define a solution. Testing cracked geometries typically requires additional material, expensive and specialist laboratory equipment and expertise in fracture mechanics. Where test data are not available the loss function (MAPE) for the cracked geometry cannot be calculated leaving the BO framework, specifically the acquisition function, struggling to rank data.

7. Conclusions

- A Bayesian optimisation framework successfully determined an array of eight material parameter values that, when applied to a ductile damage model simulation, produced an accurate representation of experimental tensile data with a mean average percentage error (MAPE) of less than 2%.
- The framework is fully autonomous requiring minimal user interaction with the combined machine learning-finite element tool typically provides calibration values in less than four hours. This compares favourably with typical time spent on trial-and-error calibration for this model.
- The ductile model parameter values are found to be non-unique and it is shown that by changing the hyperparameters of the acquisition function, different combinations of ductile damage parameters are obtained, which provide good agreement with experimental data.
- Future work will consider how the BO framework can be adapted to obtain unique model parameters.

A preprint of this research is available [41]. Additional supplementary information such as data files and code are available from zenodo <https://doi.org/10.5281/zenodo.7686217>.

8. Acknowledgements

This work was funded by the European Union through the Marie Skłodowska-Curie Actions grant number 101028291. The contributions of William Bren-

nan, a University of Limerick undergraduate student, is thanked for his contributions to earlier versions of the algorithm used in this work. We gratefully acknowledge helpful conversations with Dr. Meghana Kshiragar and Gauri Vaidya from the University of Limerick’s Lero Centre. We also thank the University of Limerick, Mathematics Applications Consortium for Science and Industry (MACSI) group for their insightful and supportive comments surrounding this research.

References

- [1] EN ISO 6892-1:2019 Metallic materials - Tensile testing - Part 1: Method of test at room temperature (ISO 6892-1:2019), 2019.
- [2] F. Abbassi, T. Belhadj, S. Mistou, A. Zghal, Parameter identification of a mechanical ductile damage using Artificial Neural Networks in sheet metal forming, *Materials & Design* 45 (2013) 605–615. doi:<http://dx.doi.org/10.1016/j.matdes.2012.09.032>.
- [3] Y. Chahboub, S. Szavai, Determination of GTN parameters for SENT specimen during ductile fracture, in: *Procedia Structural Integrity*, volume 16, Elsevier B.V., 2019, pp. 81–88. doi:[10.1016/j.prostr.2019.07.025](https://doi.org/10.1016/j.prostr.2019.07.025).
- [4] T. Zhang, K. Lu, A. Mano, Y. Yamaguchi, J. Katsuyama, Y. Li, A novel method to uniquely determine the parameters in Gurson–Tvergaard–Needleman model, *Fatigue & Fracture of Engineering Materials & Structures* 44 (2021) 3399–3415. doi:[10.1111/ffe.13568](https://doi.org/10.1111/ffe.13568).

- [5] T. Bismukhametov, J. Jäschke, Combining machine learning and process engineering physics towards enhanced accuracy and explainability of data-driven models, *Computers & Chemical Engineering* 138 (2020) 106834. doi:[10.1016/j.compchemeng.2020.106834](https://doi.org/10.1016/j.compchemeng.2020.106834).
- [6] J. Snoek, H. Larochelle, R. P. Adams, Practical Bayesian Optimization of Machine Learning Algorithms, in: *Advances in Neural Information Processing Systems*, volume 25, Curran Associates, Inc., 2012.
- [7] P. G. Mongan, V. Modi, J. W. McLaughlin, E. P. Hinchy, R. M. O’Higgins, N. P. O’Dowd, C. T. McCarthy, Multi-objective optimisation of ultrasonically welded dissimilar joints through machine learning, *Journal of Intelligent Manufacturing* 33 (2022) 1125–1138. doi:[10.1007/s10845-022-01911-6](https://doi.org/10.1007/s10845-022-01911-6).
- [8] X. Liu, C. E. Athanasiou, N. P. Padture, B. W. Sheldon, H. Gao, A machine learning approach to fracture mechanics problems, *Acta Materialia* 190 (2020) 105–112. doi:[10.1016/j.actamat.2020.03.016](https://doi.org/10.1016/j.actamat.2020.03.016).
- [9] J. Hegde, B. Rokseth, Applications of machine learning methods for engineering risk assessment – A review, *Safety Science* 122 (2020) 104492. doi:[10.1016/j.ssci.2019.09.015](https://doi.org/10.1016/j.ssci.2019.09.015).
- [10] I. Dewancker, M. McCourt, S. Clark, Bayesian Optimization for Machine Learning : A Practical Guidebook, arXiv:1612.04858 [cs] (2016). [arXiv:1612.04858](https://arxiv.org/abs/1612.04858).
- [11] F. Ghavamian, Accelerating finite element analy-

- p>sis using machine learning (2021). doi:
- [10.4233/uuid:015bbf35-5e29-4630-b466-1a29d4c5bfb3](https://doi.org/10.4233/uuid:015bbf35-5e29-4630-b466-1a29d4c5bfb3)
- .
- [12] S. Ryan, J. Berk, S. Rana, B. McDonald, S. Venkatesh, A bayesian optimisation methodology for the inverse derivation of viscoplasticity model constants in high strain-rate simulations, *Defence Technology* 18 (2022) 1563–1577. doi:[10.1016/j.dt.2021.10.013](https://doi.org/10.1016/j.dt.2021.10.013).
 - [13] Y. Zhang, D. W. Apley, W. Chen, Bayesian Optimization for Materials Design with Mixed Quantitative and Qualitative Variables, *Scientific Reports* 10 (2020) 1–13. doi:[10.1038/s41598-020-60652-9](https://doi.org/10.1038/s41598-020-60652-9).
 - [14] T. R. C. Chuaqui, A. T. Rhead, R. Butler, C. Scarth, A data-driven Bayesian optimisation framework for the design and stacking sequence selection of increased notched strength laminates, *Composites Part B: Engineering* 226 (2021) 109347. doi:[10.1016/j.compositesb.2021.109347](https://doi.org/10.1016/j.compositesb.2021.109347).
 - [15] A. Borowska, H. Gao, A. Lazarus, D. Husmeier, Bayesian optimisation for efficient parameter inference in a cardiac mechanics model of the left ventricle, *International Journal for Numerical Methods in Biomedical Engineering* 38 (2022) e3593. doi:[10.1002/cnm.3593](https://doi.org/10.1002/cnm.3593).
 - [16] H. Wankerl, C. Wiesmann, L. Kreiner, R. Butendeich, A. Luce, S. Sobczyk, M. L. Stern, E. W. Lang, Directional emission of white light via selective amplification of photon recycling and Bayesian optimization of multi-layer thin films, *Scientific Reports* 12 (2022) 5226. doi:[10.1038/s41598-022-08997-1](https://doi.org/10.1038/s41598-022-08997-1).

- [17] B. Gunn, I. T. Hettiarachchi, M. Johnstone, V. Le, D. Creighton, L. Preston, Improving high value manufacturing with simulation-based Bayesian Optimisation, in: 2022 IEEE International Systems Conference (SysCon), 2022, pp. 1–8. doi:[10.1109/SysCon53536.2022.9773798](https://doi.org/10.1109/SysCon53536.2022.9773798).
- [18] M. Abendroth, M. Kuna, Identification of ductile damage and fracture parameters from the small punch test using neural networks, Engineering Fracture Mechanics 73 (2006) 710–725. doi:[10.1016/j.engfracmech.2005.10.007](https://doi.org/10.1016/j.engfracmech.2005.10.007).
- [19] D. Chen, Y. Li, X. Yang, W. Jiang, L. Guan, Efficient parameters identification of a modified GTN model of ductile fracture using machine learning, Engineering Fracture Mechanics 245 (2021) 107535. doi:[10.1016/j.engfracmech.2021.107535](https://doi.org/10.1016/j.engfracmech.2021.107535).
- [20] W. C. Young, R. Budynas, Roark’s Formulas for Stress and Strain (7th Edition), McGraw-Hill Professional Publishing, New York, USA, UNITED STATES, 2001.
- [21] W. Wcislik, Experimental determination of critical void volume fraction f_F for the Gurson Tvergaard Needleman (GTN) model, Procedia Structural Integrity 2 (2016) 1676–1683. doi:[10.1016/j.prostr.2016.06.212](https://doi.org/10.1016/j.prostr.2016.06.212).
- [22] V. Tvergaard, A. Needleman, Analysis of the cup-cone fracture in a round tensile bar, Acta Metallurgica 32 (1984) 157–169. doi:[10.1016/0001-6160\(84\)90213-X](https://doi.org/10.1016/0001-6160(84)90213-X).

- [23] B. Shahriari, K. Swersky, Z. Wang, R. P. Adams, N. de Freitas, Taking the Human Out of the Loop: A Review of Bayesian Optimization, *Proceedings of the IEEE* 104 (2016) 148–175. doi:[10.1109/JPROC.2015.2494218](https://doi.org/10.1109/JPROC.2015.2494218).
- [24] C. E. Rasmussen, C. K. I. Williams, *Gaussian Processes for Machine Learning*, *Adaptive Computation and Machine Learning*, MIT Press, Cambridge, Mass, 2006.
- [25] C. E. Rasmussen, *Gaussian Processes in Machine Learning*, in: O. Bousquet, U. von Luxburg, G. Rätsch (Eds.), *Advanced Lectures on Machine Learning: ML Summer Schools 2003, Canberra, Australia, February 2 - 14, 2003, Tübingen, Germany, August 4 - 16, 2003, Revised Lectures*, *Lecture Notes in Computer Science*, Springer, Berlin, Heidelberg, 2004, pp. 63–71. doi:[10.1007/978-3-540-28650-9_4](https://doi.org/10.1007/978-3-540-28650-9_4).
- [26] J. Wang, *An Intuitive Tutorial to Gaussian Processes Regression*, 2022. [arXiv:2009.10862](https://arxiv.org/abs/2009.10862).
- [27] C. Zhu, R. H. Byrd, P. Lu, J. Nocedal, Algorithm 778: L-BFGS-B: Fortran subroutines for large-scale bound-constrained optimization, *ACM Transactions on Mathematical Software* 23 (1997) 550–560. doi:[10.1145/279232.279236](https://doi.org/10.1145/279232.279236).
- [28] R. Kiran, K. Khandelwal, Gurson model parameters for ductile fracture simulation in ASTM A992 steels, *Fatigue & Fracture of Engineering Materials & Structures* 37 (2014) 171–183. doi:[10.1111/ffe.12097](https://doi.org/10.1111/ffe.12097).

- [29] E. D. Meade, Experimental Study & Multiscale Modelling of the High Temperature Deformation of P91 under Multiaxial Loading, Ph.D. thesis, University of Limerick, 2020.
- [30] D. Systemes, Abaqus/CAE User's Guide - SIMULIA User Assistance 2021, Dassault Systemes, 2021.
- [31] F. Pedregosa, G. Varoquaux, A. Gramfort, V. Michel, B. Thirion, O. Grisel, M. Blondel, P. Prettenhofer, R. Weiss, V. Dubourg, J. Vanderplas, A. Passos, D. Cournapeau, M. Brucher, M. Perrot, É. Duchesnay, Scikit-learn: Machine Learning in Python, *Journal of Machine Learning Research* 12 (2011) 2825–2830.
- [32] G. De Ath, R. M. Everson, A. A. M. Rahat, J. E. Fieldsend, Greed is Good: Exploration and Exploitation Trade-offs in Bayesian Optimisation, *ACM Transactions on Evolutionary Learning and Optimization* 1 (2021) 1–22. doi:[10.1145/3425501](https://doi.org/10.1145/3425501). [arXiv:1911.12809](https://arxiv.org/abs/1911.12809).
- [33] M. Uy, J. K. Telford, Optimization by Design of Experiment techniques, in: 2009 IEEE Aerospace Conference, 2009, pp. 1–10. doi:[10.1109/AERO.2009.4839625](https://doi.org/10.1109/AERO.2009.4839625).
- [34] S. Fraley, M. Oom, B. Terrien, J. Zalewski, 14.1: Design of Experiments via Taguchi Methods - Orthogonal Arrays, in: *Chemical Process Dynamics and Controls*, 2020.
- [35] A. N. O'Connor, C. M. Davies, S. J. Garwood, The influence of constraint on fracture toughness: Comparing theoretical T₀ shifts in master

- curve analyses with experimental data, *Engineering Fracture Mechanics* 275 (2022) 108857. doi:[10.1016/j.engfracmech.2022.108857](https://doi.org/10.1016/j.engfracmech.2022.108857).
- [36] M. Abbasi, M. Ketabchi, H. Izadkhah, D. H. Fatmehsaria, A. N. Aghbash, Identification of GTN model parameters by application of response surface methodology, *Procedia Engineering* 10 (2011) 415–420. doi:[10.1016/j.proeng.2011.04.070](https://doi.org/10.1016/j.proeng.2011.04.070).
- [37] G. Rousselier, Modeling of Plasticity and Ductile Fracture Physical Mechanisms and Numerical Simulation of Laboratory Specimens, Technical Report, 2019.
- [38] R. Yan, H. Xin, M. Veljkovic, Ductile fracture simulation of cold-formed high strength steel using GTN damage model, *Journal of Constructional Steel Research* 184 (2021) 106832. doi:[10.1016/j.jcsr.2021.106832](https://doi.org/10.1016/j.jcsr.2021.106832).
- [39] V. Tvergaard, Influence of voids on shear band instabilities under plane strain conditions, *International Journal of Fracture* 17 (1981) 389–407. doi:[10.1007/BF00036191](https://doi.org/10.1007/BF00036191).
- [40] W. Brocks, D. Klingbeil, G. Künecke, D.-Z. Sun, Application of the Gurson Model to Ductile Tearing Resistance, in: A. Bakker (Ed.), *Constraint Effects in Fracture Theory and Applications: Second Volume*, ASTM International, West Conshohocken, PA, 1995, pp. 232–252. doi:[10.1520/STP14638S](https://doi.org/10.1520/STP14638S).
- [41] A. O'Connor, P. Mongan, N. O'Dowd, A Machine Learning Approach to Automate Ductile Damage Parameter Selection in Finite Element Simulations, 2023. doi:[10.5281/zenodo.7620179](https://doi.org/10.5281/zenodo.7620179).